



Aeroacoustic investigations of a three-bladed single- and twin-propeller test rig

Antonio Visingardi¹, Mattia Barbarino¹, Giuseppe Ceglia¹, Fabrizio De Gregorio¹, Luca Greco², Claudio Testa², Stefano Zaghi³, Paolo Candeloro⁴, Tiziano Pagliaroli⁴, Giovanni Bernardini⁵, Caterina Poggi⁵, Federico Porcaccia⁵

¹ CIRA – Italian Aerospace Research Centre

² CNR-Institute of Marine Engineering

³ CNR-Institute of Applied Mathematics

⁴ University Niccolò Cusano

⁵ University of Roma Tre

Corresponding author: a.visingardi@cira.it

Abstract

Noise is one of the aspects that can have a highly detrimental impact on the sustainability and social acceptability of the Urban Air Mobility (UAM). This innovative means of transportation fully relies on eVTOLs, electric multirotor rotorcraft. The design of low-noise eVTOLs is a relatively new topic of research which requires an in depth understanding of the physics related to noise sources, especially multi-interactions and near-field sound propagation. The basic understanding of the interactional aerodynamics and acoustics of multirotor configurations can be made by considering a pair of rotors placed side-by-side or in tandem configuration and neglecting the presence of an airframe. In the framework of the action group RC/AG-26 “Noise Radiation and Propagation for Multirotor System Configurations”, promoted by the Rotorcraft Group of Responsables of the European GARTEUR initiative, CIRA and Univ. Cusano carried out an experimental activity in the semi-anechoic test chamber of CIRA for an isolated and twin-propeller test rig in hover, at different speeds, sense of rotation, phase shift and mutual radial distances. The paper illustrates the outcomes of the first aerodynamic and acoustic numerical comparisons carried out by CIRA, CNR-INM-IAC, and Roma Tre (RM3).

1 Introduction

Noise is one of the aspects that can have a highly detrimental impact on the sustainability and social acceptability of the Urban Air Mobility (UAM), both in terms of aircraft and required infrastructures. In particular, surveys conducted by EASA on the societal acceptability of UAM in Europe, [1], regard noise as the highest concern of respondents when UAM aircraft are used for air taxi operations. For this reason, the aeroacoustics of multirotor configurations is a topic that is gaining ever increasing interest in the aviation research community.

The design of low-noise multirotor rotorcraft is a relatively new topic of research which requires an in depth understanding of the physics related to noise sources, especially multi-interactions and near-field sound propagation. Compared to conventional helicopters the importance of the various noise sources and the influence of noise scattering can be different. In addition, the ranges of the flow regimes are substantially different: helicopters typically fly at Reynolds numbers $O(10^6)$ whereas multirotor drones, which are equipped with blades of smaller sizes, fly at Reynolds numbers $O(10^4 - 10^5)$. The main noise sources for conventional helicopters are known well, for example blade vortex interaction noise (BVI) in descent flight, but by using distributed single or co-axial rotors, the multiple interactions among rotors and the rotor-wake interactions may play an important role in the total noise signal. Ducts, wings or the fuselage may shield or scatter the noise during its propagation. In addition, broadband noise may become a dominant noise source for rotors with low tip Mach. or disturbed rotor inflow.

The basic understanding of the interactional aerodynamics and acoustics of multirotor configurations can be made by considering a pair of rotors placed side-by-side or in tandem configuration and neglecting the presence of an airframe. Many experimental and numerical investigations have been published in the recent years related to such simplified configurations, and some examples are referenced in [2], [3], [4], [5], [6], [7], [8]. They explored different distances

between the rotors and observed that, while the separation distance has a limited-to-mild effect on the thrust coefficient of the rotor, the thrust fluctuations and the noise, including both tonal and broadband components, increase dramatically as the separation distance becomes smaller.

In the framework of the Rotorcraft Group of Responsables of the European GARTEUR initiative, [9], two action groups were launched to investigate the rotor-rotor interactional aerodynamics, RC/AG-25 “Rotor - Rotor Wakes Interactions”, [10], and the aeroacoustics of multirotor configurations, RC/AG-26 “Noise Radiation and Propagation for Multirotor System Configurations”, [11]. Numerical and experimental investigations were carried out by the consortium of RC/AG-25 on a quadcopter model, without fuselage, to evaluate the effects of the layout (square, bearhug and breaststroke) and the mutual distance of the four propellers, mainly in terms of aerodynamic performance but the aeroacoustic behaviour was also studied. In particular, the aerodynamic analyses, [12], indicated that the efficiency of a diamond configuration improves by 5% in comparison with isolated rotors for non-overlapping rotor spacings, while the interactions in square alignments are detrimental for all analysed test cases with the optimum at 0.04D blade overlap. The trend was found to be more pronounced for the backward rotor tilt with intensified interactions, for which the efficiency of the diamond configuration increased by 11% at 1.2D rotor spacing. The aeroacoustic analyses, [13], indicated that, even though generated noise levels increase with reducing rotor separation, the choice of the rotor phasing has a greater influence with orthogonal phasing at 1.2D producing 6 dB less noise for the square configuration. The diamond configuration with 1.2D rotor spacing and tip-to-tip phasing was shown to be the most beneficial both aerodynamically and acoustically for analysed observers.

Concerning the RC/AG-26, CIRA and Univ. Cusano carried out an experimental activity in the semi-anechoic test chamber of CIRA for an isolated and twin-propeller test rig in hover, at different speeds, sense of rotation, phase shift and mutual radial distances. The outcomes of this activity illustrated in [14], indicated that the aerodynamic loads on each rotor in a side-by-side configuration exhibit thrust and torque reductions in comparison to the single propeller. The interaction due to the propeller vicinity reduces the thrust by about 5.5% and the torque by about 9.5%. In addition, an increment in the load fluctuations was observed by reducing the radial distance of the two propellers. The aeroacoustic measurements highlighted a higher level of noise of about 12% in the side-by-side configuration, particularly in the inlet flow and side zones in the ranges $[180^\circ; 220^\circ]$ and $[310^\circ; 350^\circ]$.

The present paper illustrates the outcomes of the first numerical comparisons carried out by CIRA, CNR-INM-IAC, and Roma Tre (RM3) with the experimental database, produced by CIRA and the University Niccolò Cusano, on isolated and twin propeller configurations described in [14].

2 Description of the acoustic and PIV set-up

2.1 Rotor Rig

A specific setup was designed to characterize the acoustic signature of a multirotor drone. The tests were performed in a semi-anechoic chamber at the Italian Aerospace Research Centre (CIRA), Figure 1, to eliminate background noise interference. The chamber has dimensions of 5.65 x 4.45 x 4 m and a cut-off frequency of 90 Hz. The Univ. Cusano Rotor rig consists of two KDE-CF155-TP 115.5x5.3 three-bladed propellers characterized by a diameter $D=393.7$ mm and a medium chord $c=28.5$ mm. The resulting rotor solidity value is equal to $\sigma=0.138$. The propeller blade geometry is reported in Figure 2 in terms of radial distributions of chord c , thickness T_{hk} , and blade pitch β .



Figure 1: Rotor rig set-up in the CIRA semi-anechoic test chamber

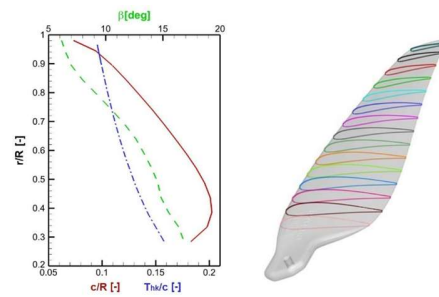


Figure 2: KDE-CF155-TP Propeller geometry.



The propellers were driven by two brushless motors type KDE4012XF-400 connected to a dedicated electronic speed controller (ESC) model KDEXF-UAS55. A custom system was implemented to control the propellers rotational speed using an NI PXI-1031 with motion controller NI-PXI-7350 and multifunction DAQ NI PXI-6259.

The speed of the propellers and the relative position of the blades were measured by means of a Kubler 05.2400 incremental encoder with 500 pulses per revolution (PPR). The propellers, motors, and encoder were mounted on a specific vertical aluminium support structure. In order to investigate the effect of the phase control between the two propellers on the pressure field, a synchrophaser was designed and implemented. The relative phase angle between the two propellers is defined in Figure 3.

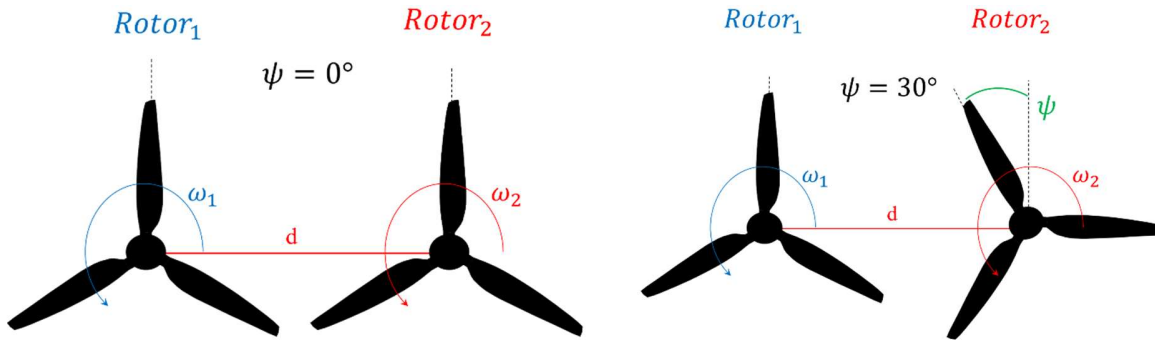


Figure 3: Definition of the phase angle between the propellers.

To measure the propeller aerodynamic loads, the Kubler encoders were removed and the motors were fixed to the ATI Mini 40 balance. The measurements were carried out at a sampling frequency of 1000 Hz for a time of 20 seconds. Mean force and moments were evaluated together with the standard deviation.

The resulting rotor rig configuration is shown in Figure 4. Only the loads of the main rotor, rotor#1, were measured, the secondary rotor was mounted on a dummy balance to preserve the symmetry of the rotor rig. The absence of the encoder decreased the accuracy of the rotational speed control. A single microphone in the proximity of the propellers monitored the rotational speed of the rotors.

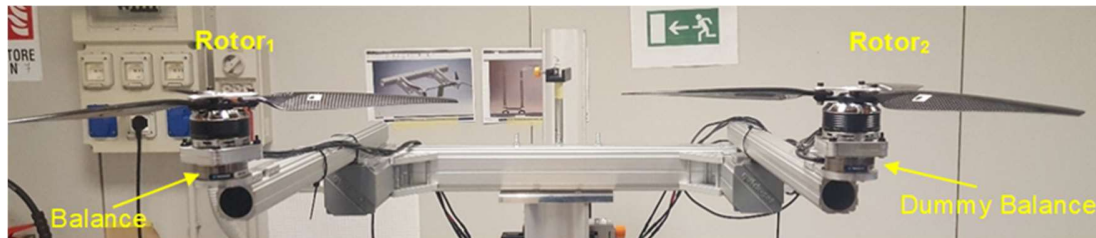


Figure 4: Rotor rig equipped with 6 components load cells

2.2 Acoustic set-up

The acoustic measurements were carried out using a moving microphone circular array consisting of eight G.R.A.S. 40PK CCP microphones and spanning the entire circumference, with an angular resolution of 10° . The microphones were positioned at a distance of $5D$ from the midpoint between the two rotors, where D is the rotor diameter. Each microphone is characterized by a frequency range from 20 to 20000 Hz and a dynamic range from 26 to 145 dB(A). The pressure time histories were acquired using a National Instruments NI cDAQ-9174 data acquisition board with a sampling frequency of 12800 Hz and an acquisition time of 30 s. A sketch of the setup employed is shown in Figure 5. The experimental tests were performed at two rotational speeds: $\Omega_1 = 5200RPM$ and $\Omega_2 = 3500RPM$ considering three values for the rotors mutual distance: $d=1.02D$, $d=1.1D$, and $d=1.2D$, respectively. The effect of reversing the sense of rotation of the secondary propeller was tested in some cases. The phase angle between the propellers varied in the range of $\psi = 0^\circ - 105^\circ$. In addition to these test cases, two additional configurations for the phase shift were considered, referred to as "random", where the slave motor follows the master motor by oscillating around an equilibrium value with a sinusoidal law and a fixed maximum amplitude of 10° .



Figure 5: Experimental setup diagram inside the anechoic chamber. The circumference on which the microphones were positioned and the definition of the polar angle Θ are also shown.

2.3 PIV experimental layout

The rotor downwash characteristics were measured by two-component Particle Image Velocimetry (2C-PIV) measurement systems. The set-up was composed of a CFR 400 dual-head Nd-Yag laser with a pulse energy of 180 mJ at a wavelength of 532 nm and a repetition rate of 10 Hz. A system of two sCMOS cameras was installed consisting of two ILA.PIV.sCMOS CLHS. The cameras were installed on a two-axis linear traversing system, to increase the measured region by horizontally shifting the cameras. The investigation of both the isolated propeller and the tandem configurations drove the installation of the two cameras side-by-side and vertically aligned to follow the wake evolution along the axial direction down to more than 1 rotor diameter, Figure 6. For the isolated propeller, the measured region of interest covered radially the wake in the range between $x=0.23 R$ to $x=1.17 R$ and vertically from $z=0.1 R$ to $z=-2.05 R$, while for the tandem configuration, a larger region is recorded ranging between $x=0.5 R$ to $x=1.75 R$ along the x -direction and in the range comprised from $z=0.09 R$ to $z=-2.06 R$ in the vertical direction. As tracer particles, aerosolized diethylhexylsebacate (DEHS) oil with a size of less than $1 \mu\text{m}$ was used. The PIV images were pre-processed by applying a background grey-level subtraction. PivView v3.6.5 (by PivTech GmbH) was used to process the particle images. The particle image analysis consisted of an iterative multigrid cross-correlation algorithm. The results presented a vector step of $\Delta x=1.43 \text{ mm}$. Considering the current values for the optical resolution (11.21 px/mm) and the laser double-pulse delay ($45\text{--}60 \mu\text{s}$), a velocity error of ϵ_u of $\sim 0.2 \text{ m/s}$ to 0.15 m/s was estimated. A complete description of the measurement setup and a discussion of the preliminary experimental results was given by De Gregorio et al. in [15].

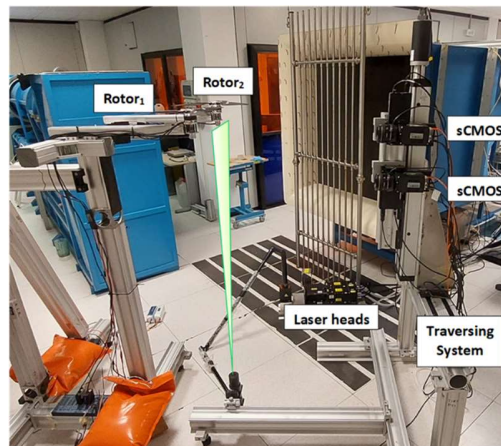


Figure 6: Experimental Layouts: 2C-PIV (from De Gregorio et al. [15] with permission).

3 Description of the methodologies for the numerical simulations

The numerical simulations were performed by the partner applying in-house-developed computational tools, of different degree of fidelity, and validated through comparisons with the experimental data produced during the AG26 project. The list of the numerical solvers is summarized in Table 1 and a detailed description is provided in the following.



Partner	Code	Description
CIRA	RAMSYS + ACO-suite	Unsteady, inviscid and incompressible free-wake Boundary Element Method (BEM) + Ffowcs Williams-Hawkings (FW-H)
CNR	CNR	Unsteady, inviscid and incompressible free-wake Boundary Element Method (BEM); Reynolds Averaged Navier-Stokes (RANSE) + Ffowcs Williams-Hawkings (FWH) + Bernoulli (BEA)
Roma Tre University	RM3	Unsteady, inviscid and incompressible free-wake Boundary Element Method (BEM) + Ffowcs Williams-Hawkings (FW-H)

Table 1: Main Characteristics of the codes used by the partners

3.1 CIRA

The CIRA aerodynamic simulations were carried out by using the medium-fidelity code RAMSYS, [16], which is an unsteady, inviscid and incompressible free-wake vortex lattice boundary element methodology (BEM) solver for multirotor, multi-body configurations developed at CIRA. It is based on Morino's boundary integral formulation, [17], for the solution of Laplace's equation for the velocity potential ϕ . The surface pressure distributions are evaluated by applying the unsteady version of Bernoulli equation, which is then integrated to provide the forces and moments on the configuration and the surrounding obstacles. A computational acceleration is obtained by applying the module for symmetrical flows and geometries implemented in the solver and the parallel execution via the OpenMP API.

The ACO-FWH solver is used for computing the acoustic free-field generated by the rotor blades. It is based on the FW-H formulation, [18], described in [19], [20] and [21]. The advanced-time formulation of Farassat 1A is employed, and the linear terms (the so-called thickness and loading noise contributions) are computed through integrals on the moving blades' surface (impermeable/rigid surface formulation). The computational acceleration is obtained by a parallel execution via the MPI API. The simulation of the aeroacoustic free-field was carried out by using the aerodynamic database evaluated by RAMSYS, and consisting of the rotor blade pressure distributions.

3.2 Roma Tre University (ROMA3)

The RM3 aerodynamic and aeroacoustic analyses rely on tools developed by the Roma Tre University unit in the last twenty years and widely validated in the past in helicopter and tiltrotor configurations, [22] and [23]. The aerodynamic module is based on the boundary integral formulation for the velocity potential presented in [24], suited for helicopter configurations where blade-vortex interaction (BVI) occurs. This formulation is fully 3D, can be applied to bodies with arbitrary shape and motion, and allows the calculation of both wake distortion and blade pressure field. It assumes the potential field to be divided into an incident field, generated by doublets over the wake portion not in contact with the trailing edge (far wake), and a scattered field, generated by sources and doublets over the body and doublets over the wake portion very close to the trailing edge (near wake). This procedure allows to overcome the instabilities arising when the wake comes too close to or impinges on the body. Recalling the equivalence between the surface distribution of doublets and vortices, the contribution of the wake portion experiencing BVI (far wake) is expressed in terms of thick vortex (i.e., Rankine vortices) distributions. The shape of the wake can be either assigned (prescribed-wake analysis) or obtained as a part of the solution (free-wake analysis) by a time-marching integration scheme in which the wake is moved accordingly to the velocity field computed from the potential solution. Once the potential field is known, the Bernoulli theorem yields the pressure distribution on the body that, in turn, is used both to determine the aerodynamic loads and as an input to the aeroacoustic solver to predict the radiated noise. The aeroacoustic analysis is performed by a prediction tool based on the Ffowcs Williams-Hawkings equation (FWH), [18]. The solution of the FWH equation is achieved through the boundary integral representation known as the Farassat Formulation 1A, [25].

3.3 CNR-INM-IAC

Aerodynamics and aeroacoustics rely on fully validated solvers developed at CNR within several EU and national research projects on marine/aeronautical configurations powered by rotating wings, [26], [27], [28], and wind turbine applications, [29]. Aerodynamics is based on a 3D, unsteady, free-wake aerodynamic formulation for the analysis of the 3D flow past rotating wings, under the assumption of incompressible, irrotational, potential flows. The numerical code UPSILON solves Laplace's equation for the perturbation velocity by a Boundary Integral Equation Method for the velocity potential accounting for the presence of the rotor via a superposition of singularities distributed on the



blade(s) surface and wake(s). The Bernoulli equation yields blade(s) pressure distribution, through which rotor thrust and torque are computed. Viscous terms are (roughly) estimated by assuming that, at each blade section, the boundary layer behaves like that over an equivalent flat plate working at the same Reynolds number. A robust free-wake solution procedure is adopted to determine the rotor wake shape by aligning wake points to the local velocity due to the advance speed (if any), rotor and wake (self-induction). The latter is computed by the Biot-Savart law coupled with a Rankine vortex-core model, [27], [29]. As a higher-fidelity solver, Xnavis, that is based on the integration of the Reynolds Averaged Navier–Stokes equations (RANSE) in the frame of reference fixed to the rotor, is proposed. It uses the Spalart-Allmaras one-equation model for the eddy viscosity computation; the governing equations are discretized by a conservative cell-centred finite volume approach, on a multi-block structured body-fitted grid with partial overlapping. More details can be found in [30]. In the framework of potential aerodynamics, pressure fluctuations in the flow field are directly provided by the Bernoulli equation combined with the Biot–Savart law, [27]. Throughout the paper, it is used for validation purposes only, at microphones located very-near the emitting surface(s) to avoid troubles with the acoustic delays. Aeroacoustics relies on the solution of the Ffowcs Williams-Hawkings (FWH) Acoustic Analogy by a Boundary Element Method (BEM) of zeroth order. The FWH equation is integrated by assuming the rotor blades as acoustic surfaces - 1A Farassat formulation, [25] - or by following the permeable surface approach (FWH-P) that has proven to be a valuable way to account for the sources of sound localized in the flow field. In this paper FWH-1A results are obtained by using the blade(s) pressure distributions coming from the potential aerodynamics whereas RANSE data detect the sources of sound upon the permeable surface in the case of FWH-P outcomes.

4 Test cases selected for the numerical simulations

The test cases selected for the numerical simulations, Table 2, deal with an isolated propeller rotating counter-clockwise at two speeds: 3500 RPM and 5200 RPM, and a set-up of twin counter-clockwise co-rotating propellers, rotating at 5200 RPM, installed at the same height and three different radial distances from each other: $d/D = 1.02$; 1.10 and 1.20, where D represents the propeller diameter. In addition, the effect of reversing the sense of rotation of the secondary propeller (Hov#18, clockwise rotating), or de-phasing it with respect to the main one (Hov#15, +60° de-phase) has been also evaluated.

Hover condition	d/D	$\Delta\phi$ [°]	Density [kg/m ³]	SoS [m/s]
Hov#01 (SP)	-	-	1.198	344.75
Hov#02 (TP)	1.02	0	1.198	344.75
Hov#12 (TP)	1.10	0	1.222	343.23
Hov#14 (TP)	1.20	0	1.222	343.23
Hov#18 (TP) – contra-rotating	1.20	0	1.222	343.23
Hov#15 (TP)	1.20	60°	1.222	343.23

Table 2: Test cases selected for the numerical simulations

5 Results of the numerical simulations

5.1 Aerodynamic performance

The BEM numerical simulations were carried out by using the space and time discretization indicated in Table 3:

Partner	Panels per Blade	Azimuth step [°]	Revolutions	Wake spirals
CIRA - RAMSYS	2100	2°	8	8
CNR - UPSILON	3400	2°	7	6
Roma Tre - RM3	6000	3°	10	6

Table 3: Space and time discretization for the aerodynamic simulations

Figure 7 shows CIRA RAMSYS results of the thrust coefficient time history during the last revolution of both the single and twin propeller system to highlight the load and its fluctuations produced by the three-bladed propellers. Table 4 reports the percentage ratio RMS/CT_{avg} for all the test cases investigated.

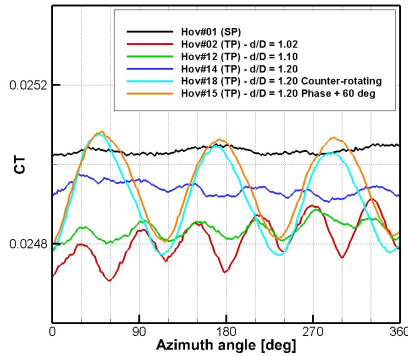


Figure 7: Time histories of the thrust coefficient during the last revolution – RAMSYS simulations

Test Case	d/D	CT avg	RMS	RMS/CT avg %
Hov#01 (SP)	-	0.0250344	4.09E-06	0.02
Hov#02 (TP)	1.02	0.0248094	5.04E-05	0.20
Hov#12 (TP)	1.10	0.0248350	2.21E-05	0.09
Hov#14 (TP)	1.20	0.0249380	1.61E-05	0.06
Hov#18 (TP) - counter rotating	1.20	0.0249118	9.05E-05	0.36
Hov#15 (TP) - 60 deg phase	1.20	0.0249488	9.05E-05	0.36

Table 4: CT fluctuations for the rotor rig

The thrust coefficient of the isolated propeller is produced by an almost steady flow field. It has been multiplied by two to be used as a reference for a direct comparison with the loads of the two-propeller system. Passing to the twin propellers co-rotating and in phase, Hov#02 to Hov#14, 6/rev fluctuations can be observed, which are the result of the interactional effects between the two propellers. Their amplitude decreases as the distance between the two propellers increases. For the cases at $d/D = 1.20$, the opposite sense of rotation and the 60° de-phasing of the secondary propeller produce high 3/rev fluctuations only. This is because, for these two test conditions only, there is a 3/rev perfect alignment of the two propellers' blades along the horizontal inter-axis line ($\psi = 270^\circ$ for the main propeller and $\psi = 90^\circ$ for the secondary propeller, according to Figure 3), which produces the maximum interactional effect.

Figure 8 shows the time-averaged thrust and torque values of the investigated test cases. The isolated propeller displays higher values of both the thrust and torque coefficients when compared to the twin propellers.

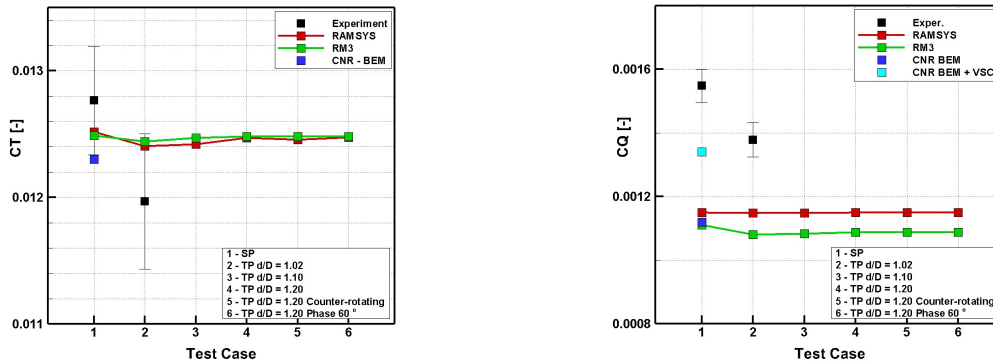


Figure 8: Time-averaged thrust and torque values of the investigated test cases

An explanation for this behaviour was identified by Zarri et al.,[8], in the sudden breakdown of the coherent vortical structures that were instead observed to develop downstream of the single propeller. Figure 9 illustrates the loss of coherence in the wake structure produced by the propeller-propeller interactions.

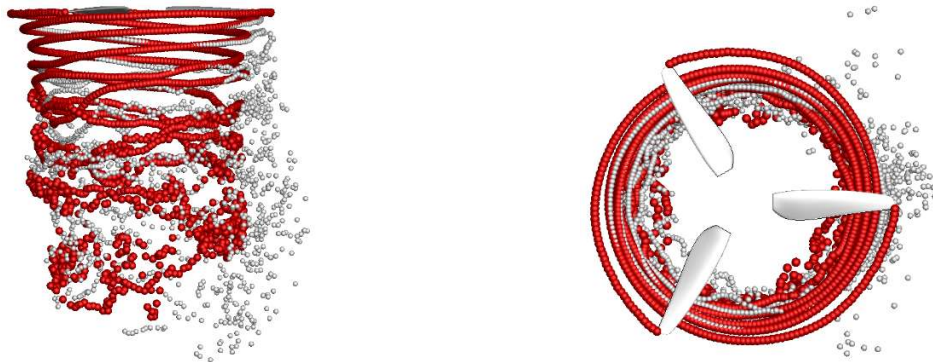


Figure 9: Loss of coherence in the wake structure produced by the propeller-propeller interactions at $d/D = 1.02$, grey spheres, compared to the coherent structure of the isolated propeller wake – red spheres. RAMSYS simulations - XZ view (left) and XY view (right)

With respect to the experimental measurements, BEM solvers predict a lower thrust coefficient for the isolated propeller (RAMSYS: 1.95%; RM3: 2.16%), and a higher estimation for the twin propellers at $d/D = 1.02$ (RAMSYS: 3.65%; RM3: 3.94%). However, for both predictions these values fall within the experimental fluctuations. A slightly lower prediction (3.3% with respect to experiments) is observed for the isolated propeller from the CNR BEM solver. As expected, by increasing the radial distance between the two propellers the reduction in thrust reduces suggesting an asymptotic trend of the twin propellers to reach the thrust coefficient of the signal propeller as the d/D ratio increases. As for the time fluctuations, at $d/D = 1.20$ the sense of rotation and the de-phasing produce only minor differences in the time-averaged thrust coefficient with respect to the baseline condition Hov#14. The inviscid torque is almost insensitive to the different installations. The significant discrepancy with the experimental measurement is produced by the inviscid nature of the BEM solvers. The viscous correction applied to the CNR BEM solver reduces the underestimation, as shown in Figure 8.

PIV measurements were carried out by CIRA to evaluate the details of the propellers' downwash in terms of the vertical component w of the velocity induced by the wake system. These measurements enabled a more exhaustive validation of the numerical solvers but also represented the opportunity for CIRA to extend the PIV field of investigation downstream of the propeller disks, which in the literature are usually limited to no more than one rotor radius. A detailed description of the investigation procedure combined with a Γ_2 vortex detection criterion can be found in [33]. The PIV measurements were elaborated both in instantaneous and time-averaged maps. The latter one was used to extract the vertical component w of the velocity induced at several distances from the propellers' disks as shown in Figure 10.

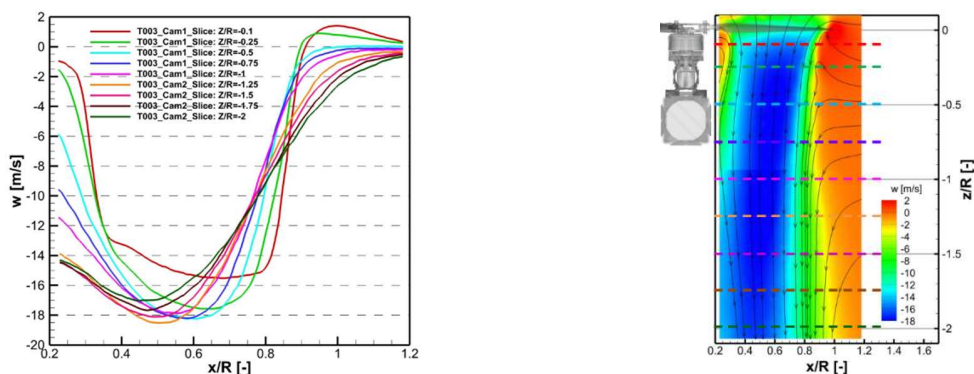


Figure 10: Time-averaged PIV measurements - Radial distributions of the vertical component of the induced velocity (left) at several heights below the propeller disks (right)

Numerical vs experimental comparisons of the radial distribution of the w component of the induced velocities are presented for all test cases. Regarding the isolated propeller, the 3500 RPM and 5200 RPM speeds were investigated. All the comparisons were limited to a distance of one radius due to the limitations of the potential solvers to accurately predict the experimental velocity field far from the rotor disk.

Four main regions can be identified in the induced velocity maps: the propeller hub region; the maximum acceleration below the disk; the shear layer boundary and slope; and the blade tip region. In the hub region, since no hub was modelled in the solvers, the main differences arise for the different root cut-out radial station selected.

Figure 11 and Figure 12 illustrate the results for the isolated propeller at 3500 RPM and 5200 RPM, respectively. RANSE computations were available for the first speed only. The maximum acceleration down the propeller disk is similarly estimated by all the solvers with the exception of the $z/R = -1.00$ station where the BEM simulations predict a higher velocity compared to RANSE simulations and the experimental data. This occurrence gives a measure of the low-dissipative nature of the potential solvers. Regarding the shear layer region, the differences with respect to the experimental results are explained by the diffusion produced by the viscous effects, which causes a marked thickening and reduced slope of the experimental shear layer moving downstream from the rotor disk, and which is instead modelled in the BEM solvers by using vortex core models. Their selection and fine tuning are a key point for a correct modelling of the wake shape and the viscous effects on the velocity field. To this extent, the applied potential solvers show a similar behaviour, with the position slightly ahead of the experimental data at the lower positions below the propeller disk. The RANSE solver is excessively diffusive closer to the propeller disk but is in better agreement with the experiment in the lowermost position. The region around the blade tip ($r/R = 1$) shows that the potential solvers predict a larger upwash which is not observed in the experimental results. Differently, RANSE outcomes are generally in fairly good agreement with the experiment.

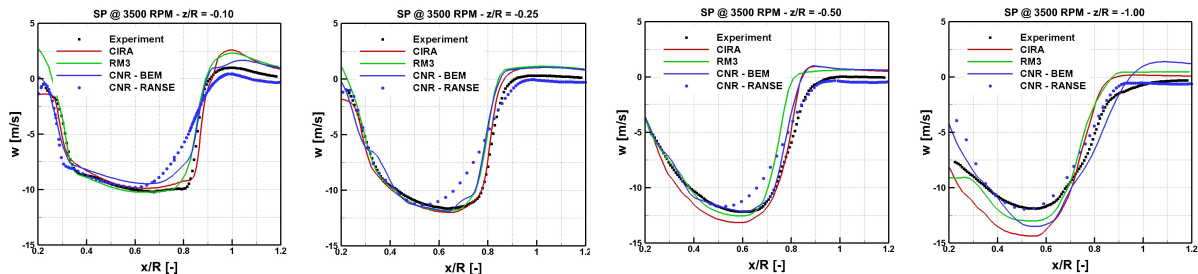


Figure 11: Single propeller @ 3500 RPM - Radial distributions of the vertical component of the induced velocity at four heights below the propeller disks: $z/R = -0.10$; -0.25 ; -0.50 and -1.00

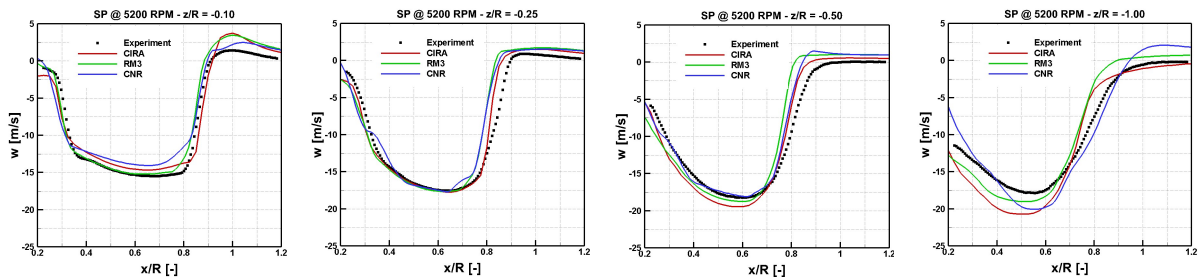


Figure 12: Single propeller @ 5200 RPM - Radial distributions of the vertical component of the induced velocity at four heights below the propeller disks: $z/R = -0.10$; -0.25 ; -0.50 and -1.00

The analysis of the velocities induced by the twin propellers, Figure 13, generally confirms the trends observed for the isolated propeller. The maximum acceleration down the propeller disks shows the tendency to be higher than the experiment, especially for the lowermost position and especially for RAMSYS results. The tip-to-tip region, around $r/R = 1$, shows a higher upwash in the numerical prediction at the first three vertical stations. For the case at $z/R = -1$, RAMSYS results predict higher accelerations, whereas the converse is true for the RM3 solver. One interesting behaviour for the case at $d/D = 1.20$ is the shift to the right of the experimental velocity peak position which is not followed by the predictions up to $z/R = -0.5$ and which is followed only by RM3 results at $z/R = -1$. This could be explained by the global meandering of the wake system produced by the strong mutual interactions between the wakes of the two propellers.

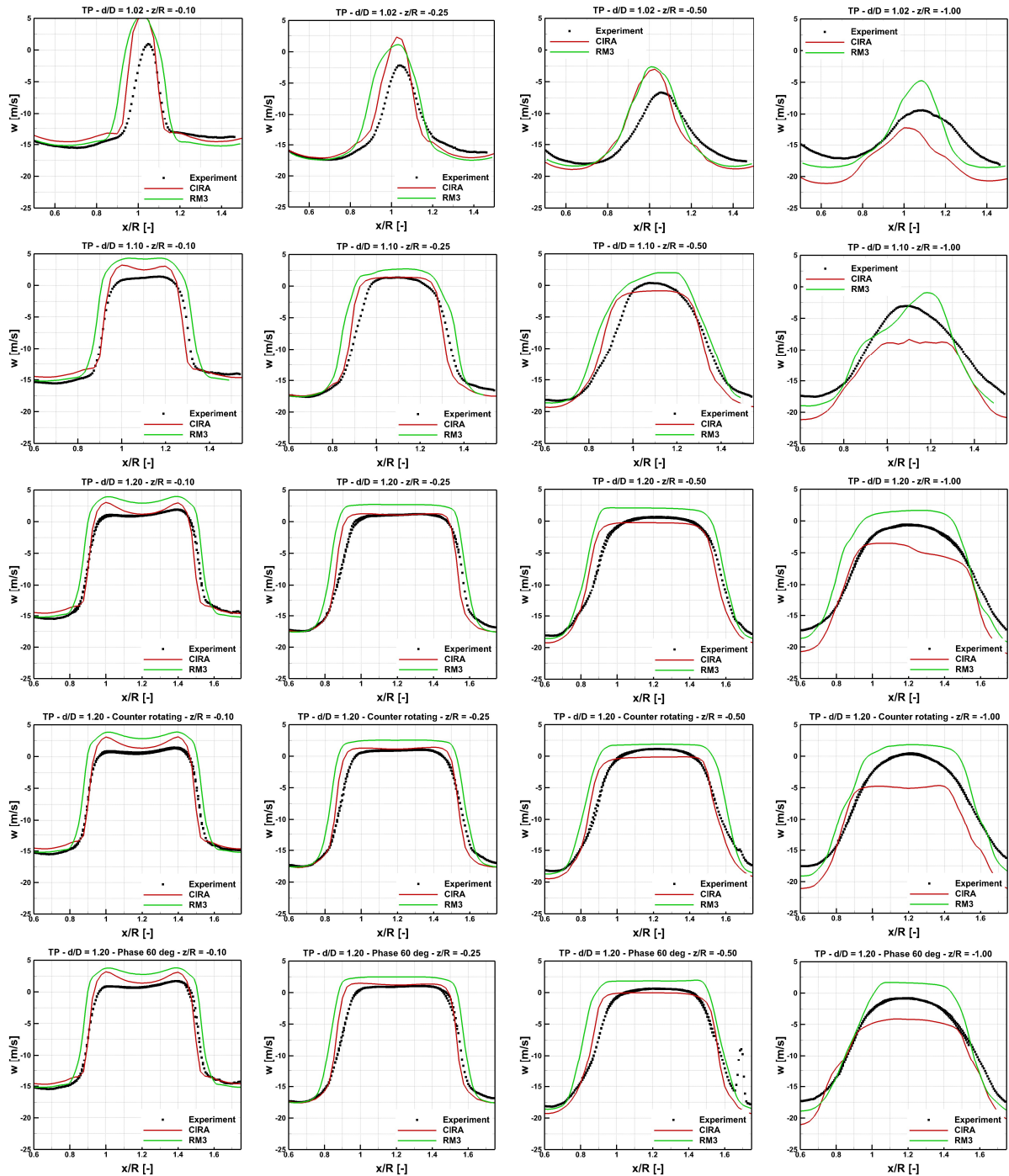


Figure 13: Twin propellers -Radial distributions of the vertical component of the induced velocity at four heights below the propeller disks: $z/R = -0.10; -0.25; -0.50$ and -1.00

5.2 Aeroacoustic performance

First, aeroacoustics results are shown for the isolated rotor at 3500 RPM by comparing the pressure signals from Bernoulli and FWH acoustic analogy relying on both the 1A and permeable-based approaches. Herein, RANSE+FWH-P solvers are used to assess the interpolating procedure between CFD and acoustic surface grids, in view of the further use of a Large-Eddy-Simulation (LES) to detach the main sources of sound on and past the rotor



blades. In addition, even in the presence of quick, undesirable smearing out effects of the vorticity/turbulent field downstream of the rotor, the RANSE+FWH-P solution yields preliminary information on the role of nonlinear terms moving away from the rotor disk. CFD domain is 1.2D long upstream of the rotor whereas the outflow is 3.75D far downstream. Lateral boundaries are indeed 2.5D far from the rotor axis, whereas the porous surface S, chosen as a cylinder with generatrix line coincident with the propeller axis, is 1.9D long (upstream and outflow caps are 0.39D and 1.52D far from the disk, respectively) with a radius of 0.58D. CFD mesh consists of 14M cells whereas the porous surface is discretized by approximatively 29K BEM panels. Note that acoustic results are insensitive to further panels refinements. As shown in Figure 14, a set of seven microphones 0.61D far from the centre line of S, ranging from 0.25D upstream to 0.5D downstream (with a step of 0.125D), and placed in the most refined zone of the CFD domain are considered. It is proven that the placement of S complies with the best-practise discussed in [31] and [32]. Pressure fluctuations upstream of the rotor disk (not shown here for conciseness) show an excellent agreement among potential-based solvers, yielding a typical tonal-like shape. The FWH-P solution is very close to this wave-shape so that nonlinear effects may be considered as negligible. On the disk plane, MIC3, Figure 15-left, the quality of the comparison among Bernoulli, FWH-1A and FWH-P signals is the same. Here, the blade(s) governs the mechanisms of noise generation, and in turn, the radiated noise. Note that MIC3 is located in the most refined CFD zone where grid overlapping occurs. Thus, a direct comparison between RANSE and FWH-P pressures (for validation purposes of the aerodynamic dataset exchange for aeroacoustics) is consistent. As shown, the agreement is very good even in the presence of higher-frequency oscillations in the RANSE solution. Moving down-stream, the FWH-1A formulation captures pressure signals similar to those predicted by Bernoulli up to MIC4; moving on, wake effects induce a change of the wave-shape. The difference between FWH-1A and FWH-P results is a measure of the nonlinear acoustic terms. This behaviour is exacerbated at MIC7, Figure 15-right, where the vorticity field constrained on a (free) 2D surface no longer represents the real wake evolution: as a result, Bernoulli signals are completely different from FWH-1A results that, in turns, are different from FWH-P outcomes. The linear terms are observed to decay moving far away from the disk, but their effect is still present one radius downstream, being reduced by the porous contribution.

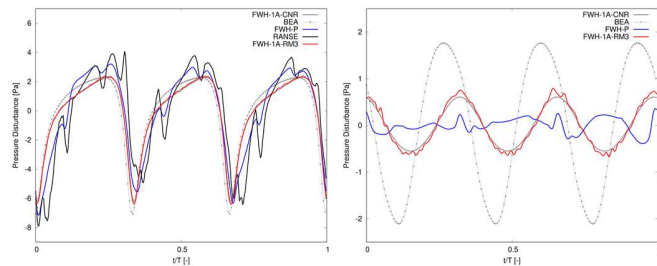
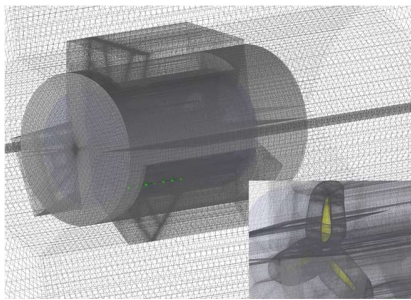


Figure 14: CFD grid blocks and zoom nearby the rotor Figure 15: Time-history of the pressure signals predicted at MIC3 (left) and MIC7 (right)

Then, Figure 16 compares the sound directivity from numerical solvers with experiments at the first two BPFs in the microphone set of Figure 5 for the entire set of selected test cases shown in Table 2. For the isolated propeller at 3500RPM, the agreement among FWH-1A based results is excellent even though they underestimate the noise level with respect the FWH-P polar plot (about 2 dB at 0° and 180°). As expected, for this low rotational Mach (≈ 0.2) nonlinear terms affect the noise signature by the sources of sound past the blades. Experimental directivity at the first BPF of the co-rotating twin propellers approaches that of the isolated one as the distance between the propeller hubs increases, except in microphones located back from the rotor disc (namely 270°), where the twin propellers exhibit higher SPL values. Numerical results obtained by different partners for the isolated propellers and the co-rotating twin propellers are in good agreement. They also match well with the experimental data at the first BPF. However, some differences appear in specific regions, particularly in front of the rotor (90° microphones), where numerical results underestimate SPL values by up to 10-20 dB, and behind the rotor (270° microphones), where discrepancies can reach 30-40 dB. The accuracy of numerical predictions slightly improves over experimental data when considering contra-rotating twin-propellers and co-rotating ones with a 60° phase shift. Indeed, in these cases, the numerical results accurately predict the directivity of the first BPF in front of the rotor disk and underestimate SPL values by 10-20 dBs in the rear region (with a 10-20 dB improvement over the previous cases). However, a SPL overestimation of about 10-15 dB is noticed on microphones located on the port side and 5 dB on the starboard side in the latter configuration (see Figure 5 for microphone locations). For the second BPF, one can observe that the experimental data show SPL values equal to or higher than those at the first BPF, even for the isolated rotor configuration for which, due to the axis-symmetry of the flow, one would have expected a dominant contribution of the first BPF. The matching with



experiments degrades for the second BPF directivity where relevant discrepancies reach 10-20 dB everywhere, especially for the isolated rotor. Note that the differences in the polar plots, upstream and downstream of the rotor disk between CIRA-RM3 and CNR are due to the negative values of SPLs that have been forced to zero in the directivity patterns. At this stage, it is believed that the low SPL values predicted by CIRA, RM3 and CNR come only from residual numerical fluctuations of the acoustic signals that do not show BVI phenomena (neither by BEM nor RANSE simulations) and inherently do not model any fluid-structure interaction that might occurs between the wake structure and experimental set-up. The presence of such important second BPFs in the experimental data, even in the case of an isolated rotor, would suggest that the presence of the two propeller pylons in the experimental setup as well as the possible presence of reflection phenomena due to the acoustically reflective floor of the test chamber, Figure 5, not included in the numerical analysis, could be the cause of these.

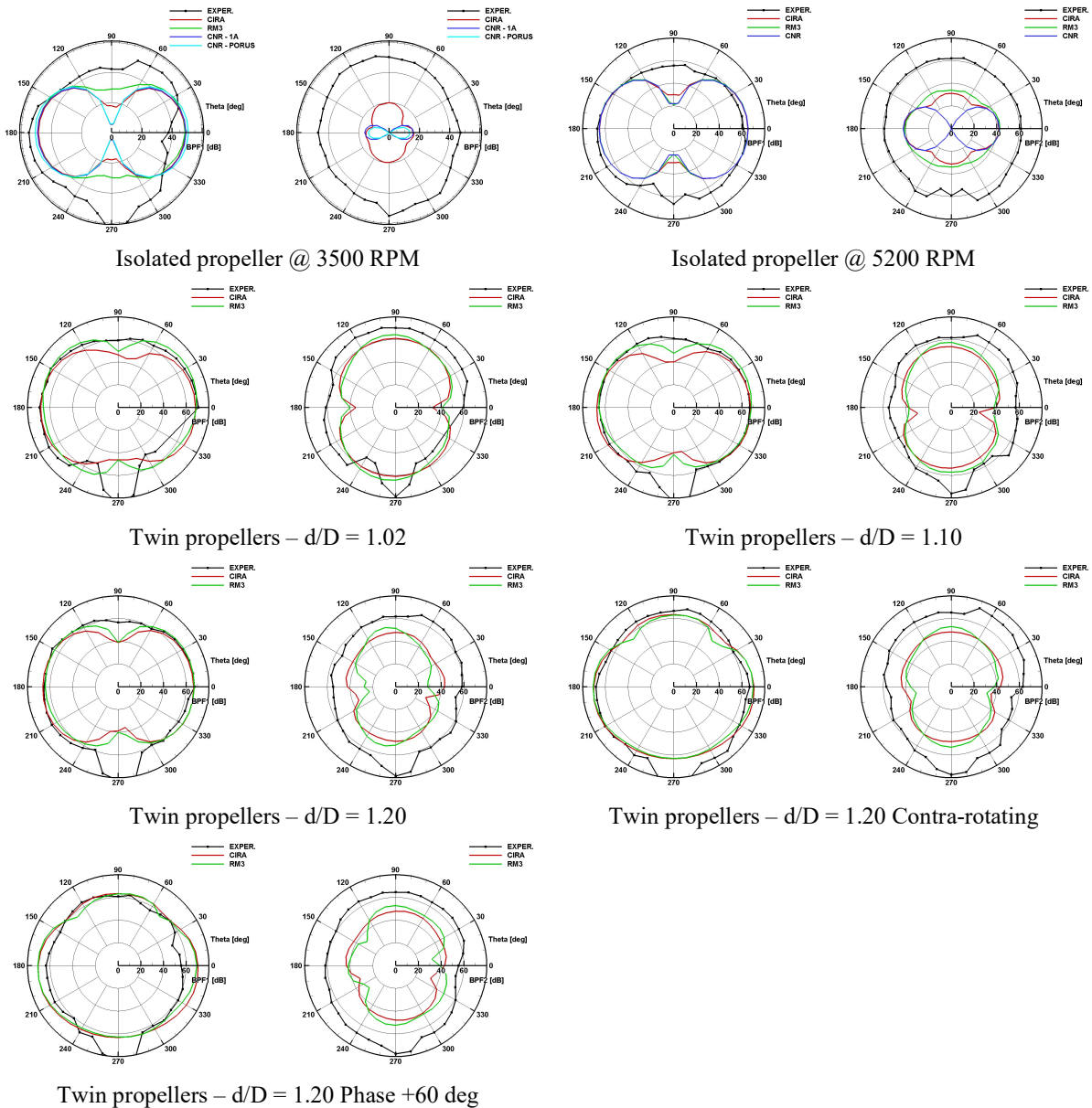


Figure 16: SPL polar diagrams – Numerical-experimental comparisons – BPF1 and BPF2



6 Conclusions

In the framework of the GARTEUR RC/AG-26: “Noise Radiation and Propagation for Multirotor System Configurations”, CIRA and Univ. Cusano carried out an aerodynamic and acoustic experimental activity for an isolated and twin-propeller test rig in hover, at different speeds, sense of rotation, phase angles and mutual radial distances. The database produced was applied by CIRA, CNR and Roma Tre for first numerical aerodynamic and acoustic validations. In-house developed aerodynamic and acoustic solvers, based on the BEM methodology and the FW-H formulation, respectively, were applied by the authors. In addition, only for the isolated propeller at 3500 RPM, CNR applied a RANSE solver coupled to the permeable surface approach FWH-P.

The aerodynamic investigations highlighted the following aspects: the analysis of the thrust coefficient CT time histories during the last revolution shows that the isolated propeller produces an almost steady flow field. Conversely, the twin propellers generate an unsteady flow field that produces fluctuations in the CT with an amplitude decreasing as the distance between the two propellers increases. In particular, 6/rev fluctuations are observed for the cases with the two propellers in phase, whereas marked 3/rev fluctuations are observed when propellers are contra-rotating or 60° de-phased: in these two cases the blades are fully aligned and there is a maximum in the interaction.

The isolated propeller produces the highest average value of the CT. Passing to the twin-propeller configuration, the CT of each of the two propellers reduces because of a loss of coherence of the wake system with respect to the isolated propeller. By increasing the distance between the two propellers the CT recovers and tends to approach the isolated propeller’s value. The reversed sense of rotation of the secondary propeller at $d/D = 1.20$ produces a slightly lower value with respect to the case of co-rotating propellers. The numerical results predict an average CT which falls within the experimental fluctuation. Numerical underestimations in the torque coefficient CQ are due to the inviscid nature of the solvers applied. The viscous correction in the CNR BEM improves the estimation.

PIV measurements were produced by CIRA, which were applied to investigate the capability of the aerodynamic solvers to capture the details of the wake development. The predicted w component of the induced velocities turns out to be in good agreement with the experiment up to about $r/R = 0.50$. Further downstream, the excessive acceleration in the downwash predicted by the BEM solvers is mainly produced by the less dissipative nature of the wake vortex core models applied. Instead, the RANSE solver is capable of correctly estimating the downwash up to one radius below the disk ($r/R = 1.0$).

Aeroacoustic experiments showed, for each configuration examined, first and second BPF harmonics of the same order of magnitude, with the first BPF directivity of the co-rotating twin propellers approaching that of the isolated one as the distance between the propeller hubs increases, except in microphones located in the rotor wake region, where the twin propellers exhibit higher SPL values. The analysis of the isolated rotor at 3500 RPM highlights volume sources-induced effects on the noise directivity, causing an increase of approximately 2 dB of the dipole-like lobes. At 5200 RPM, the numerical predictions from the different partners match well. They also well correlate with the experimental data at the first BPF, except for the area in front of the rotor, where numerical results underestimate SPL values by up to 10-20 dB, and in the propeller wake region, where discrepancies can reach up to 30-40 dB. However, numerical predictions capture the directivity change of the first BPF, which is present in the experimental data due to both the phase shift and the reversal of the direction of rotation of one of the two propellers (contra-rotating configuration). The accuracy slightly improves in these latter cases, even though, underestimations of 10-20 dBs are still present in the area of the propeller wakes and, in the case of co-rotating twin propellers with phase shift, an overestimation of the order of 10 dBs on the starboard and port sides. Finally, numerical results highly underpredict the magnitude of the second BPF, showing differences of about 20 dBs in all examined cases.

It is necessary to understand the reasons for such relevant discrepancies between numerical and experimental results, and to further investigate the role of nonlinearities in the noise prediction by a higher fidelity CFD analysis of the flow past the rotor. All these open questions will be faced throughout the ongoing activity of the Action Group AG26.

Acknowledgements

The numerical and experimental investigations described in the present paper were all carried out by the authors in the framework of the GARTEUR Action Group 26: “Noise Radiation and Propagation for Multirotor System Configurations” promoted by the Rotorcraft Group of Responsables.



References

- [1] EASA. Study on the societal acceptance of Urban Air Mobility in Europe. May 2021;
- [2] Zhou, W., Ning, Z., Li, H., Hu, H. An experimental investigation on rotor-to-rotor interactions of small UAV propellers. *Proceedings of the 35th AIAA Applied Aerodynamics Conference*, Denver, CO, USA, 5–9 June 2017; p. 3744. <https://doi.org/10.2514/6.2017-3744>;
- [3] Shukla, D.; Komerath, N. Multirotor Drone Aerodynamic Interaction Investigation. *Drones*. 2018, 2, 43. <https://doi.org/10.3390/drones2040043>.
- [4] Ko, J.; Kim, J.; Lee, S. Computational study of wake interaction and aeroacoustic characteristics in multirotor configurations. *INTER-NOISE and NOISE-CON Congress and Conference Proceedings*. Institute of Noise Control Engineering: Reston, VA, USA, 2019; Volume 259, pp. 5145–5156;
- [5] Bu, H., Wu, H., Bertin, C., Fang, Y., Zhong, S. Aerodynamic and acoustic measurements of dual small-scale propellers. *Journal of Sound and Vibration*. <https://doi.org/10.1016/j.jsv.2021.116330>, 2021;
- [6] Stokkermans, T.; Usai, D.; Sinnige, T.; Veldhuis, L. Aerodynamic interaction effects between propellers in typical eVTOL vehicle configurations. *Journal of Aircraft*. 2021, 58, 815–833. <https://doi.org/10.2514/1.C035814>;
- [7] Zanotti, A.; Algarotti, D. Aerodynamic interaction between tandem overlapping propellers in eVTOL airplane mode flight condition. *Aerospace Science and Technology*. 2022, 124, 107518. <https://doi.org/10.1016/j.ast.2022.107518>;
- [8] Zarrì, A., Dell’Erba, E., Munters, W., Schram, C. Aerodynamic installation effects on the sound emissions of a drone in hover. *Proceedings of DICUAM 2022*. March 22-24, 2022.
- [9] <https://garteur.org/> ;
- [10] Boisard, R., et al. Rotor - Rotor Wakes Interactions – Terms of Reference for the GARTEUR Action Group RC/AG-25. Feb. 2019;
- [11] Yin, J., et al. Noise Radiation and Propagation for Multirotor System Configurations - Terms of Reference for the GARTEUR Action Group RC/AG-26. Dec. 2021;
- [12] Kostek, A., Braukmann, J.N., Löble, F., Miesner, S., Visingardi, A., Boisard, R., Riziotis, V., Keßler, M., Gardner, A.D. Experimental Investigation of Quadrotor Aerodynamics with Computational Cross-Validation. *Proceedings of the Vertical Flight Society’s 79th Annual Forum & Technology Display*. West Palm Beach, FL, USA, May 16–18, 2023;
- [13] Kostek, A., Braukmann, J.N., Löble, F., Miesner, S., Visingardi, A., Boisard, R., Riziotis, V., Keßler, M., Gardner, A.D. Experimental and Computational Investigation of Aerodynamic Interactions in Quadrotor Configurations. *Journal of the American Helicopter Society*. Vol.69, 022009 (2024), DOI:10.4050/JAHS.69.022009;
- [14] Nargi, R.E., Candeloro, P., De Gregorio, F., Ceglia, G., Pagliaroli, T., Fluid-Dynamic and Aeroacoustic Characterization of Side-by-Side Rotor Interaction., *Aerospace*, vol.10, pg. 851, 2023, <https://doi.org/10.3390/aerospace10100851>;
- [15] De Gregorio, F., Candeloro, P., Ceglia, G., Pagliaroli, T. Flow field and acoustic assessment of twin rotors in hover conditions. *XXXI AIVELA Annual Meeting*, Milan, IT, December 5-6, 2023;
- [16] Visingardi, A., D’Alascio, A., Pagano, A., Renzoni, P. Validation of CIRA’s rotorcraft aerodynamic modelling system with DNW experimental data. *22nd European Rotorcraft Forum*, Brighton, UK, 1996. doi: <http://hdl.handle.net/20.500.11881/3171>;
- [17] Morino, L. A General Theory of Unsteady Compressible Potential Aerodynamics. NASA CR-2464, 1974;
- [18] Ffowcs Williams J. E., Hawkings D. L., Sound generation by turbulence and surfaces in arbitrary motion, *Philosophical Transactions of the Royal Society of London*. Series A, Mathematical and Physical Sciences 264: 321-342. <https://doi.org/10.1098/rsta.1969.0031>;
- [19] Casalino D. An advanced time approach for acoustic analogy predictions, *Journal of Sound and Vibration*, 261 (4) (2003) 583-612. doi: [https://doi.org/10.1016/S0022-460X\(02\)00986-0](https://doi.org/10.1016/S0022-460X(02)00986-0);
- [20] Casalino D., Barbarino M., Visingardi A., Simulation of helicopter community noise in complex urban geometry. *AIAA Journal*, 49 (8) (2011) 1614-1624. doi:10.2514/1.J050774;



DICUAM 2024, 22-24 March 2024

- [21] Barbarino M., Petrosino F., Visingardi A. A high-fidelity aeroacoustic simulation of a VTOL aircraft in an urban air mobility scenario. *Aerospace Science and Technology* (2021). 107104. 10.1016/j.ast.2021.107104;
- [22] Gennaretti, M., Bernardini, G., Serafini, J., & Romani, G. (2018). Rotorcraft comprehensive code assessment for blade–vortex interaction conditions. *Aerospace Science and Technology*, 80, 232-246;
- [23] Gennaretti, M., Colella, M., and Bernardini, G., Prediction of tiltrotor vibratory loads with inclusion of wing-proprotor aerodynamic interaction, *Journal of Aircraft*, Vol. 47, No. 1, 2010, pp. 71–79;
- [24] Gennaretti, M., and Bernardini, G. Novel boundary integral formulation for blade-vortex interaction aerodynamics of helicopter rotors. *AIAA journal*, 2007, Vol. 45, No. 6, pp. 1169–1176;
- [25] Farassat, F., Derivation of Formulations 1 and 1A of Farassat, 2007;
- [26] Leone, S., Testa, C., Greco, L., Salvatore, F., 2013. Computational analysis of self-pitching propellers performance in open water. *Ocean Engineering*. 64, 122–134;
- [27] Greco, L., Muscari, R., Testa, C., Di Mascio, A., 2014. Marine propellers performance and flow-field features prediction by a free-wake panel method. *J. Hydrodyn. Ser. B (Engl. Ed.)* 26 (5);
- [28] Testa, C., Greco, L., Bosschers, J., 2022. Marine propeller shaft loading analysis in moderate oblique-flow conditions. *Ocean Eng.*, 262;
- [29] Greco, L., Testa, C., 2021. Wind turbine unsteady aerodynamics and performance by a free-wake panel method. *Renewable Energy* 164, 444–459;
- [30] Zaghi, S., Muscari, R., Di Mascio, A. Assessment of blockage effects in wind tunnel testing of wind turbines, *Journal of Wind Engineering and Industrial Aerodynamics*, 2016, 154, 1-9;
- [31] Testa, C., Porcacchia, F., Zaghi, S., Gennaretti, M., 2021. Study of a FWH-based permeable-surface formulation for propeller hydroacoustics. *Ocean Engineering*, 240, 109828;
- [32] Testa, C., Porcacchia, F., Muscari, R., Greco, L. Noise field properties of marine propellers in open water, *Ocean Engineering*, 288 (Part 2), 2023, 116194;
- [33] De Gregorio, F., Visingardi, A., Iuso, G. An Experimental-Numerical Investigation of the Wake Structure of a Hovering Rotor by PIV Combined with a Γ_2 Vortex Detection Criterion, *Energies*. 2021, 14, 2613. <https://doi.org/10.3390/en14092613>.